Characteristics and frequency of weak stellar impulses of the Oort cloud

John J. Matese[1,2]

Jack J. Lissauer[2]

[1]Department of Physics, University of Louisiana at Lafayette

Lafayette, LA, 70504-4210

[2]Space Science Division, MS 245-3, NASA Ames Research Center

Moffett Field, CA, 94035

[1] Tel: (337) 482 6697; Fax: (337) 482 6699; E-mail: matese@louisiana.edu

Pages: 40 including 2 cover sheets, 26 text pages, 12 figures

Submitted to the journal ICARUS on April 9, 2001.

PROPOSED RUNNING HEAD

"Stellar impulses of the Oort cloud"

EDITORIAL CORRESPONDENCE AND PROOFS

John J. Matese

Department of Physics

University of Louisiana at Lafayette

Lafayette, LA, 70504-4210

(Between May 15 - August 10, 2001, correspondence to

Space Science Division, MS 245-3 NASA Ames Research Center, Moffett Field, CA, 94035)

Abstract: We have developed a model of the response of the outer Oort cloud of comets to simultaneous tidal perturbations of the adiabatic galactic force and a stellar impulse. The six dimensional phase space of near-parabolic comet orbital elements has been subdivided into cells. A mapping of the evolution of these elements from beyond the loss cylinder boundary into the inner planetary region over the course of a single orbit is possible. This is done treating each perturbation separately, and in combination, during a time interval of 5 Myr. We then obtain the time dependence of a wide range of observable comet flux characteristics, which provides a fingerprint of the dynamics. These include the flux distributions of energy, perihelion distance, major axis orientation and angular momentum orientation. Correlations between these variables are also determined. We show that substantive errors occur if one superposes the separately obtained flux results of the galactic tide and the stellar impulse rather than superposing the tidal and impulsive perturbations in a single analysis. Detailed illustrations are given for an example case where the stellar mass and relative velocity have the ratio $M_\star/V_{rel} = 0.043$ $M_\odot$/km s^{-1} and the solar impact parameter is 45 000 AU. This case has features similar to the impending Gliese 710 impulse with the impact parameter selected to be close to the low end of the predicted range. We find that the peak in the observable comet flux exceeds that due to the galactic tide alone by $\approx 41\%$. We also present results for the time dependence of the flux enhancements and for the mean encounter frequency of weak stellar impulse events as functions of $M_\star/V_{rel}$ and solar impact parameter.

Key Words: comets, dynamics; celestial mechanics.

1. INTRODUCTION

The outer Oort cloud is formally defined as the ensemble of comets having semimajor axes $\geq 10^4$ AU (Oort 1950). It has been shown that the vast majority of these comets are first-time entrants into the inner planetary region (Fernandez 1981), and such comets are therefore commonly referred to as *new*. The dominance of the galactic tide in making Oort cloud comets observable has been firmly established. Beginning with the work of Byl (1983), a succession of studies (cf. Matese and Whitman 1992, Wiegert and Tremaine 1999, and references therein) have demonstrated that the distribution of observed orbital elements of new comets correlates well with the predictions of a theory that the galactic disk tide is the predominant force responsible for changing comet perihelia and bringing them into the observable zone. This is true during the present epoch and is likely to be true when averaged over long time scales (Heisler *et al.* 1987, Heisler 1990).

Nonetheless, stellar impulses do contribute to making Oort cloud comets observable, and we investigate herein the circumstances where the *combined* perturbations of the stellar impulse and the galactic tide are important. Our focus therefore is on weak showers, defined here as cases where the peak observable shower flux is less than $2\times$ the flux due to the adiabatically varying tide alone. The strongest stellar showers, or storms, will occur when the star perturbs the inner Oort cloud, whose properties are less well known (Stern and Weissman 2001, Levison *et al.* 2001).

Our dynamical analysis is described in Section 2. It contains the description of the effects of the galactic tidal forces and of a hypothetical stellar impulse acting on near-parabolic Oort cloud comets. Section 3 gives our results. First we calculate the peak flux enhancement and the mean encounter frequency as functions of $M_\star/V_{rel}$ and solar impact parameter. We then compare predictions when the galactic and stellar interactions are treated separately and the fluxes are combined (superposed-flux case) with those when the interactions are combined and a single flux calculation is done (superposed-perturbations case). Choosing a specific example which has some aspects of the impending Gliese 710 close approach (García Sánchez *et al.* 1999), we give detailed predictions of time-dependent distributions for various orbital elements, including

correlations between them. These characteristics constitute a fingerprint of weak impulsive perturbations of the Oort comet cloud. We then present a listing of the principal consequences of weak showers having a wide range of stellar masses, velocities and impact parameters. This section is concluded by comparing our results with some prior analyses. In Section 4 we summarize our predictions, discuss observations and comment on the possibility of discerning an impulsive contribution to the comet flux.

2. DYNAMICAL MECHANISMS

2.1. Galactic Tide

The dynamics of the galactic tide acting on near-parabolic Oort cloud comets is most simply given in a Newtonian framework (Matese and Whitmire 1996). This framework describes how the angular momentum and the perihelion distance ($H \approx \sqrt{2GM_{\odot}q}$, $\mathbf{H} \perp \mathbf{q}$) are changed by the galactic tide. Let $\mathbf{F}$ be the galactic tidal force acting on a comet separated from the Sun by $\mathbf{R} = \mathbf{X} + \mathbf{Y} + \mathbf{Z}$. Here $\mathbf{X}$ points to the center of the galaxy and $\mathbf{Z}$ points to the north galactic pole (NGP). In the conventional approximation, at the solar location the galactic potential is taken to be azimuthally symmetric and the velocity curve is radially flat. The tidal force in a non-rotating frame whose axes point to the galactic center and NGP at the time of observation can then be modeled as (Heisler and Tremaine 1986) $\mathbf{F} = {\Omega_{\circ}}^2\mathbf{X} - {\Omega_{\circ}}^2\mathbf{Y} - {\Omega_z}^2\mathbf{Z}$, where $\Omega_{\circ}$ is the solar orbital frequency about the galactic core and $\Omega_z = \sqrt{4\pi G\langle\rho\rangle}$ is the nominal solar angular oscillation frequency about the galactic midplane. Here $\langle\rho\rangle$ is the azimuthal average of the local disk density. The galactic tidal torque on the comet-Sun system is $\dot{\mathbf{H}} = \mathbf{R} \times \mathbf{F}$.

We denote the original value of semimajor axis, prior to perturbation by the planets, as A. The original orbital energy parameter is $x \equiv 10^6 \mathrm{AU}/A$. Our choice of the remaining five independent orbital elements includes the time of passage of perihelion, τ, the aphelion latitude, B, and longitude, L, the magnitude of the comet's specific angular momentum, H, and its orientation angle, α, which is defined in Eq. (3) below.

Near-parabolic comets are most likely to have their perihelia reduced to the observable region. For

such comets, $\mathbf{R} \approx R\hat{\mathbf{Q}}$, with cartesian aphelia unit vector components

$$\hat{\mathbf{Q}} \approx \frac{\mathbf{Q}}{2A} = (\cos B \cos L, \cos B \sin L, \sin B). \tag{1}$$

Obtaining the secular change in angular momentum over an orbital period, P_A, we have

$$\Delta\mathbf{H}^{\mathbf{tide}} = \langle\dot{\mathbf{H}}\rangle P_A \approx \frac{5}{2} P_A A^2 {\Omega_z}^2 \cos B \left[\hat{\phi} \sin B \left(1 + \epsilon \cos 2L\right) + \hat{\theta}\epsilon \sin 2L\right], \tag{2}$$

where $\hat{\phi}$, $\hat{\theta}$ are the conventional spherical unit vectors in a system of coordinates with radial direction $\hat{\mathbf{Q}}$. Estimates based on the observed distribution of luminous matter and on stellar distributions are $\Omega_\circ \equiv 2\pi/240$ Myr for the solar orbital frequency, $\langle\rho\rangle \approx 0.1$ $\mathrm{M}_\odot\mathrm{pc}^{-3}$ for the galactic disk density at the present epoch, $\Omega_z \equiv 2\pi/90$ Myr for the solar oscillation frequency about the galactic midplane, and $\epsilon \equiv {\Omega_\circ}^2/{\Omega_z}^2 \approx 0.1$ for the galactic radial tide parameter (Merrifield 1992, Holmberg and Flynn 2000). In Eq. (2), we omit a term of relative error of $\mathcal{O}\left[\left(\epsilon\, \Omega_z P_A\right)^2\right] < 0.01$ that occurs when we choose the non-rotating reference frame as we do. An error of $\mathcal{O}\left[\frac{1}{6}\left(\Omega_z P_A\right)^2\right]$ occurs when we make the adiabatic tidal approximation and assume a constant value of disk density.

Both components of the vector $\langle\dot{\mathbf{H}}\rangle$ are slowly varying since changes in the major axis orientation are

$$\cos B\, \Delta L \approx \Delta B \approx \mathcal{O}\left[\frac{\Delta H}{H}\frac{q}{A}\right] \ll 1$$

during a single orbit. In contrast, because $\mathbf{H}$ itself is rapidly changing, any formalism which secularly averages the scalar time derivative

$$\dot{H} = H^{-1}\left(\mathbf{H}\cdot\dot{\mathbf{H}}\right) = H^{-1}\left(H_\phi \dot{H}_\phi + H_\theta \dot{H}_\theta\right) \equiv -\cos\alpha\, \dot{H}_\phi - \sin\alpha\, \dot{H}_\theta \tag{3}$$

(as in Heisler and Tremaine 1986) will find $\langle\dot{H}\rangle$ to be rapidly varying since α is rapidly changing. This highlights the value of the Newtonian presentation. Equation (3) reduces to the parabolic limit of the

corresponding result in Heisler and Tremaine (1986; their Eq. (20)) if one sets the core interaction parameter $\epsilon = 0$ and transforms the angles B, L, α, to the more conventional Euler angles ω, Ω, i. The latter set are all rapidly varying during a single orbit.

2.2. Stellar Impulse

The dynamics of a hypothetical high-speed star interacting with the Sun-comet system on a rectilinear trajectory is now considered. We take the relative velocity to be the same for both the Sun and comet and we treat the interaction as instantaneous for all comets since the transit time for a star with velocity ≈ 30 km s^{-1} through the Oort cloud is $\approx 30\,000$ yr, which is small compared to the time scale for changes in the flux of comets into the planetary region resulting from the impulse. The conventional definition of the impact parameter is adopted. It is directed from the scattering center (the star) to the scattered object (the comet or Sun) at the respective closest approach. Symbol notation is as follows:

Stellar mass :	$M_\star$
Solar impact parameter :	$\mathbf{b}_\odot$
Comet position at impulse :	$\mathbf{R}$
Stellar velocity relative to the Sun (comet) :	$\mathbf{V_{rel}}$
Comet impact parameter :	$\mathbf{b} \equiv \mathbf{b}_\odot + \mathbf{R} - (\mathbf{R} \cdot \hat{\mathbf{V}}_\mathbf{rel})\hat{\mathbf{V}}_\mathbf{rel}$
Stellar position at comet impulse :	$\mathbf{r} \equiv \mathbf{R} - \mathbf{b}$
Comet orbital velocity :	$\mathbf{V}$
Comet specific angular momentum :	$\mathbf{H} \equiv \mathbf{R} \times \mathbf{V}$

where $\mathbf{b}_\odot \perp \mathbf{V_{rel}}$, $\mathbf{b} \perp \mathbf{V_{rel}}$. The impulse to the comet (relative to that on the Sun) is then

$$\Delta\mathbf{V} = -\frac{2GM_\star}{V_{rel}}\left[\frac{\mathbf{b}}{b^2} - \frac{\mathbf{b}_\odot}{{b_\odot}^2}\right],$$

$$\mathbf{\Delta H^{impulse}} = \mathbf{R} \times \mathbf{\Delta V} \tag{4}$$

with components

$$\Delta H_\theta{}^{impulse} = \frac{2\mathrm{G}M_\star R}{V_{rel}} \left[\frac{b_\phi}{b^2} - \frac{b_{\odot\phi}}{b_\odot{}^2} \right],$$

$$\Delta H_\phi{}^{impulse} = -\frac{2\mathrm{G}M_\star R}{V_{rel}} \left[\frac{b_\theta}{b^2} - \frac{b_{\odot\theta}}{b_\odot{}^2} \right]. \tag{5}$$

Matese *et al.* (1999) note that one can neglect energy changes since

$$\frac{\Delta x^{impulse}}{x} \approx 2\Delta \left[\sqrt{\frac{q}{R}} \right]^{impulse} \ll 1,$$

which is part of the definition of our weak shower approximation.

We can estimate the parameter range of interest as follows. The weak showers we focus on occur when the impulse to shower comets preferentially dominates the impulse to the Sun. If the perturbation affects comets that have $A > 25\,000$ AU the galactic tide can contribute to reducing $H < H_{lc} \equiv \sqrt{2\mathrm{GM}_\odot q_{lc}}$. Here $q_{lc} \approx 15$ AU is the nominal loss cylinder boundary. Setting $R \approx b_\odot$, we find that comets are impulsed with $\Delta H^{impulse} > H_{lc}$ within a tube of impact parameter

$$\frac{b}{R} \approx \frac{b}{b_\odot} \approx \frac{M_\star}{\mathrm{M}_\odot} \frac{10 \text{ km s}^{-1}}{V_{rel}} < 1 \ .$$

The strength of the shower will then depend on the ratio $M_\star/V_{rel}$ and $b_\odot$ since these determine the size and the location of the impulsed tube of comets. For long-range tidal impulses, Eq. (4) reduces to

$$\mathbf{\Delta H^{impulse}} \longrightarrow \frac{2\mathrm{G}M_\star R^2}{V_{rel} b_\odot{}^2} \left[\hat{\mathbf{R}} \times \hat{\mathbf{V}}_{\mathbf{rel}} \ \hat{\mathbf{R}} \cdot \hat{\mathbf{V}}_{\mathbf{rel}} + 2\hat{\mathbf{R}} \times \hat{\mathbf{b}}_\odot \ \hat{\mathbf{R}} \cdot \hat{\mathbf{b}}_\odot \right] \tag{6}$$

and the angular momentum change is smaller by a factor $R/b_{\odot}$. Further, substantive impulses will no longer be localized along the perturber's trajectory across the celestial sphere.

Impulsed comets could be moving either inward or outward at the perturbation site. The free fall time from the location where the impulse occurred, R, of a near-parabolic comet of semimajor axis A, is given by

$$\Delta t(R,A) = \frac{P_A}{2\pi}\left\{\pi + \mathrm{Sign}(\dot{R})\left[\frac{\pi}{2} - \sin^{-1}\left(\frac{R}{A}-1\right) + \left(\frac{R}{A}\left(2-\frac{R}{A}\right)\right)^{\frac{1}{2}}\right]\right\}. \tag{7}$$

Letting $t = 0 \equiv$ the stellar impulse time, this expression gives the *observation* time of these comets which is identifiable with the perihelion passage time, τ.

2.3. Combined Interaction

The galactic tidal perturbation and the impulse are, in nature, superposed in the course of a cometary orbit. The galactic tide changes the angular momentum from its prior value as the comet recedes from the planetary region with $q^{prior} > q_{lc}$ and, after the stellar impulse, continues to change it until the comet enters the planetary region with its observable value

$$\mathbf{H^{obs}} = \mathbf{H^{prior}} + \mathbf{\Delta H^{pre-impulse-tide}} + \mathbf{\Delta H^{impulse}} + \mathbf{\Delta H^{post-impulse-tide}} \tag{8}$$

$$\equiv \mathbf{H^{prior}} + \mathbf{\Delta H^{impulse}} + \mathbf{\Delta H^{tide}}. \tag{9}$$

The simplest way to visualize this process is suggested by the vector sum in Eq. (9). Cometary phase space will have the prior loss cylinder distribution displaced by $\mathbf{\Delta H^{impulse}} + \mathbf{\Delta H^{tide}}$. The standard step function for the prior distribution of angular momentum is changed to a uniformly displaced distribution as illustrated in Fig. 1, which shows the angular momentum plane defined by the aphelion direction. Since the energy impulse is small, the prior energy distribution is essentially unaffected. For individual comets the impulsive change depends on B, L, x and τ (which determine $\mathbf{R}$ and $\mathbf{b}$) while the tidal change depends

only on B, L, x. Both are independent of the remaining two elements, H and α. Figure 1 illustrates that in the present modeling, the phrase "loss cylinder" might be more appropriately changed to "loss circle".

2.4. The Mapping Procedure

We first choose the stellar impulse parameters, $M_\star$, $\mathbf{b}_\odot$ and $\mathbf{V_{rel}}$. For each observation time, τ, we randomly select major axis orientations and comet energies. The sampling of orbital elements is as follows. For each of 16 values of $0 < \tau \leq 5$ Myr chosen to adequately map the time dependence of the shower, we equipartition $15 \times 36 \times 35$ cells of $-1 \leq \sin B \leq 1$, $0 \leq L < 360°$ and $10 \leq x \leq 70$. The most tightly bound comet energy included ($x = 70$) is the empirical limit for comets made observable during the weak showers considered here. A set of values for $\sin B$, L and x within each cell is then randomly chosen. This selects the four orbital elements which are essentially unchanged in the course of a single orbit. Now we can calculate $\mathbf{R}$ from Eqs. (1) and (7), and $\mathbf{b}, \mathbf{r}$ from their defining relations.

Next we specify the prior distribution of the remaining two orbital elements to satisfy the loss cylinder model. It is conventionally assumed that the *in situ* angular momentum distribution of Oort cloud comets of specified semimajor axis A can be adequately approximated as

$$\frac{d^2N}{dH_\phi dH_\theta} \propto \Theta({H_\phi}^2 + {H_\theta}^2 - {H_{lc}}^2), \tag{10}$$

where Θ is the unit step function. This is a statement that most comets which leave the planetary region with $q < q_{lc}$ have experienced impulsive energy changes from the planets which have removed them from the outer Oort cloud (Fernandez 1981). So $\mathbf{H^{prior}} = ({H_\phi}^{prior}, {H_\theta}^{prior})$ is taken to be uniformly distributed outside the loss cylinder boundary, as described in Fig. 1.

We now calculate $\mathbf{\Delta H}$ from Eqs. (2) and (5) and map $\mathbf{H^{prior}} \Longrightarrow \mathbf{H^{obs}}$ using Eq. (9). Note that this mapping constitutes a simple displacement of the angular momentum vector, which remains perpendicular to the major axis, and is uniformly applicable to the entire distribution space of $\mathbf{H^{prior}}$ for the chosen set

of elements B, L, x, and τ. This mapping is repeated in $16 \times 36 \times 35 \times 15 = 3 \times 10^5$ calculations to sample the entire phase space. We can then determine the region of the loss cylinder that has been refilled by the perturbation. Subdividing the loss cylinder into 15×24 equal-area cells of $H < H_{lc}$ and α, as defined in Eq. (3), we then record the orbital elements if the phase space cells are refilled. Figure 1 illustrates the procedure.

We have effectively subdivided the *interior* of the loss cylinder into $15 \times 36 \times 35 \times 15 \times 24$ cells for each of 16 perihelion passage values. So the *complete* prior Oort cloud phase space ($10 \leq x \leq 70$) outside the loss cylinder has been mapped into $\approx 10^8$ cells inside the loss cylinder over the 5 Myr interval. Liouville's theorem assures us that the density of phase space points will remain conserved during the mapping. Alternative integration procedures that randomly select individual prior phase space points exterior to the loss cylinder, and dynamically evolve them forward one orbit, are substantially less efficient than the present mapping scheme in determining how the loss cylinder is refilled. The entire analysis is performed using *Mathematica* 4.0 (Wolfram 1999) on a personal computer.

3. MODELING RESULTS

We define a comet to be "observable" if $q < q_{obs} \equiv 5$ AU. The number of new comets per unit distance actually observed with perihelia between 2 and 5 AU is ≈ 11 AU^{-1}, which is half of that observed interior to 2 AU (≈ 20 AU^{-1}). The distribution decreases rapidly beyond 5 AU (Matese *et al.* 1999). It is generally argued that this is due to an observational selection effect which discriminates against observing large-q Oort cloud comets (Wiegert and Tremaine 1999). This is the only statistically significant observational selection effect applicable to new Oort cloud comets. These results are for comets with high-quality orbit determinations, specified as Class I by Marsden and Williams (2000).

Also adopted is a simple flux distribution for the Oort cloud (comets per year per energy interval that are passing perihelion), $\Phi(x) \propto x^{3/2} \left(1 - \frac{10}{x}\right)$ for $10 \leq x \leq 70$. This is an analytical approximation to the numerical results of Duncan *et al.* (1987). We use $\Phi(x)$ as a statistical weighting when a loss cylinder cell

has been refilled.

3.1. Peak flux enhancement and frequency of weak stellar showers

In Fig. 2 we show the loci of curves for $b_\odot$ versus $M_\star/V_{rel}$ over a grid containing the peak flux of observable comets (obtained in a manner described below) up to a factor of two larger than the steady state tide-alone flux. The precise predictions depend somewhat on the *in situ* prior phase space modeling, on the direction of $\mathbf{b}_\odot$, and $\mathbf{V_{rel}}$ and on the models one adopts for the loss cylinder and observable zones, but the general trends remain the same.

We next estimate the mean encounter frequency for stellar impulses of various strengths. More precisely, we use stellar mass and velocity distributions to estimate the stellar impulse rate as a function of the impact parameter, $b_\odot$, and the impulse strength parameter, $M_\star/V_{rel}$. The impulse rate of stars of specified number density and relative velocity (n, V_{rel}) within an impact parameter $b_\odot$ is $nV_{rel}\pi {b_\odot}^2$. Heisler *et al.* (1987) list the number densities and mean dispersion velocities, σ, of all stellar populations and adopt a Maxwellian speed distribution

$$p(V) = \sqrt{2/\pi}\ \frac{V^2}{\sigma^3}\ e^{-V^2/2\sigma^2}. \tag{11}$$

Here $p(V)dV$ is the probability that a randomly selected star has a speed relative to the local standard of rest within the interval V to $V + dV$. Following Heisler *et al.* we neglect the affect of the Sun's small motion relative to the local standard of rest and assume that $p(V)$ describes the distribution of stellar speeds relative to the Sun.

For a specified population subset n_i, σ_i, M_i, we integrate over all speeds giving an impulse strength stronger than some chosen lower limit $M_\star/V_{rel}$. Finally we sum over all populations to obtain the mean frequency of encounters with closest approach less than $b_\odot$ and stellar mass to encounter velocity ratio

exceeding $M_\star/V_{rel}$

$$\xi(b_\odot, M_\star/V_{rel}) = \pi {b_\odot}^2 \sum\nolimits_i n_i\ \sigma_i \int_0^{\upsilon_i} d\upsilon\ \sqrt{2/\pi}\ \upsilon^3 e^{-\upsilon^2/2}\ ,\ \text{where}\ \upsilon_i \equiv \frac{M_i/\sigma_i}{M_\star/V_{rel}}. \tag{12}$$

The limit of Eq. (12) as $M_\star/V_{rel} \longrightarrow 0$ is (Heisler *et al.* 1987)

$$\xi_{net} \equiv \lim_{M_\star/V_{rel}\to 0} \xi(b_\odot, M_\star/V_{rel}) = \pi {b_\odot}^2 \sum\nolimits_i n_i\ \bar{V}_i = \left(b_\odot/57\ 000\ \text{AU}\right)^2 \text{Myr}^{-1}, \tag{13}$$

where $\bar{V}_i = \sqrt{8/\pi}\ \sigma_i$ is the mean speed. Conversely, one sees that for large values of $M_\star/V_{rel}$, $\xi \propto {b_\odot}^2/\left(M_\star/V_{rel}\right)^4$. The probability that the time to the next encounter (interior to $b_\odot$ and stronger than $M_\star/V_{rel}$) will be greater than Δt is $\exp(-\xi\Delta t)$, and the median time to the next encounter is $\Delta t_{median} = 0.693/\xi$. Mean encounter timescales, ξ^{-1}, are illustrated in Fig. 3.

Using the a different total stellar number density and a single mean stellar speed, García-Sánchez *et al.* (1999) have predicted the frequency of all stellar encounters within a cross section of radius $b_\odot$ to be $\xi_{net} \approx \left(b_\odot/59\ 000\ \text{AU}\right)^2 \text{Myr}^{-1}$ as compared to Eq. (13).

3.2. Characteristics of a weak stellar shower distribution

The largest predicted Oort cloud perturbation in the near future ($\approx$ 1.36 Myr) is due to GL 710 (García-Sánchez *et al.* 1999). It has best fit parameters $M_\star = 0.6\ \text{M}_\odot$, $V_{rel} = 14\ \text{km s}^{-1}$ and $b_\odot =$ 69 000 AU, which according to our analysis would produce a peak flux $\approx 1.08\times$ the steady state value due to the galactic tide alone. The mean encounter timescale (interior to 69 000 AU and stronger than $0.043\ \ \text{M}_\odot/\text{km s}^{-1}$) is $\xi^{-1} = 28$ Myr. But the distance uncertainty ($\pm$ 35 000 AU) is sufficiently large that a wide range of results are possible. Integrating over impact parameters centered on 69 000 AU and circled by a Gaussian distribution with an uncertainty of 35 000 AU, we find that in 16% (50%, 84%) of the cases the impact parameter lies within 45 000 AU (75 000 AU, 110 000 AU). The corresponding mean encounter

timescale is 67 Myr (24 Myr, 11 Myr).

We illustrate the mapping procedure described in Section 2 by analyzing the "baseline" case $M_\star/V_{rel} = 0.043$ $M_\odot$/km s^{-1} with $\mathbf{V_{rel}}$ along the galactic z axis and closest approach $\mathbf{b}_\odot = 45\,000$ AU at galactic longitude 135°. This corresponds to the 1σ lower limit on the impact parameter for GL 710.

3.2.1. Time dependence of the observable shower

First we obtain the time dependence of all observable comets in both the superposed-flux and the superposed-perturbations analyses. A proper analysis of this problem requires that the tidal and impulsive contributions to $\mathbf{\Delta H}$ must both be included in a vector superposition, as indicated in Eq. (9), before proceeding with the mapping procedure. For comparison we illustrate the results one would obtain if one predicted the flux using $\mathbf{\Delta H^{tide-alone}}$ and added that to the predicted flux from $\mathbf{\Delta H^{impulse-alone}}$. The time-dependent flux (observable comets/yr, normalized to the tide-alone value) are compared in Fig. 4. During early epochs the superposed-flux analysis generally results in a slightly smaller flux than the superposed-perturbations analysis. In contrast at later epochs the superposed-flux analysis results in a substantially larger flux than the superposed-perturbations analysis. The explanation for this can be found when we investigate at the time-dependent energy distributions.

3.2.2. Refilling phase space

Figure 5 displays the energy-dependent "efficiency", $f \equiv \frac{d\dot{N}}{dx}/\Phi(x)$, which is the ratio of the observable energy-dependent flux to the maximum possible flux if all other elements of phase space $(B, L, \alpha, q < q_{obs})$ were completely refilled at the given epoch τ. The efficiency is independent of the *in situ* flux model $\Phi(x)$. Insights into the errors introduced by superposing flux can be seen in Fig. 5, where statistically forbidden efficiencies > 1 occur for small-x comets.

Figure 1 illustrates that the energy-dependent flux at a given time due to a stellar impulse can roughly

be categorized in one of three ways, depending on the semimajor axes of perturbed comets that are consistent with free-fall timing, Eq. (7).

If A is sufficiently large ($> 45\ 000$ AU), the stellar impulse is irrelevant and can be ignored since the tidal torque would be large enough to efficiently refill the loss cylinder anyway. No additional number of comets is made observable by the stellar impulse. Only the prior phase space of the comets made observable is changed. The discrepancy between the flux at later epochs in Fig. 4 corresponds to cases where the tide alone, or the impulse alone, could both make comets observable for the same values of x, B, L, τ (but for different regions of $\mathbf{H^{prior}} \rightarrow \mathbf{H^{obs}}$ in general). Therefore one gets an erroneous excess for large-A, late-arriving comets when the flux from separate analyses are combined.

If A is sufficiently small ($< 25\ 000$ AU), the galactic tide is irrelevant and can be ignored since the tidal torque is too small to be of significance. These observable comets can be considered to be directly injected by the star. No latitude signature of the galaxy is to be expected.

For intermediate values of A, the combined perturbations of the stellar impulse and the galactic tide must be considered. A weaker tide associated with an intermediate value of cometary semimajor axis A *can* be sufficient to make a comet observable if aided by a stellar impulse. Under these circumstances one would expect to see the galactic signature in this population with intermediate values of A if it is sufficiently enhanced.

3.2.3. Distributions in energy and perihelion distance

All subsequent results are for the physically realistic superposed-perturbations analysis. Figure 6 illustrates the time evolution of the observable energy flux distribution $\frac{d\dot{N}}{dx}$. We see that in the earliest epochs, before the effects of the shower are significant, the distribution peaks at $x \approx 27$. This is due to the combination of a rapidly decreasing efficiency and a rapidly increasing *in situ* flux. The tide alone is unable to make comets observable if $x > 40$ since $\mathbf{\Delta H^{tide}} \propto x^{-\frac{7}{2}}$ is a strong function of x. It is this range of comet

energies, $27 < x < 40$, where the combined effect of stellar impulse and tide is most important. The small difference in the curves of Fig. 4 at early epochs is due to this effect, which becomes more pronounced in cases where $b_{\odot} > 50\ 000$ AU and the perturbation is weaker.

We find that at $\tau = 5$ Myr the flux differs significantly from the $\tau = 0$ result only in the energy interval $22 < x < 34$. For energies $x > 34$ the orbital period is < 5 Myr and no shower contributions will occur at epochs $\tau > 5$ Myr. For $x < 22$ the efficiency, f, is essentially unaffected by the shower for all τ - see Fig. 5.

Figure 7 shows the time evolution of the perihelion distance distribution. Note that the number density of observable comets increases with increasing q, because this region of phase space is closer to the boundary of the loss cylinder and thus requires smaller perturbations to be occupied. The $\tau = 0$ results and the $\tau = 5$ Myr results are indistinguishable.

3.2.4. Distributions in the longitude and latitude of aphelion

In Fig. 8 we show the time-dependent distributions in aphelion directional angles $\sin B$ and L, which would be flat for isotropic flux. Because of the choice of stellar trajectory, the latitudinal distributions exhibit north-south symmetry as the shower rises and decays. Deficiencies at the poles and equator, which characterize the tidal interaction, are observed in the data. The $\tau = 0$ curve in L exhibits a modest variation due to the galactic radial perturbation term, ϵ. Subsequent asymmetry in L is due to the weak shower which is centered on $L = 135°$.

If these predictions are to be compared with observations, aphelion directions can be associated with antipodal directions of the observed perihelia vectors. There is negligible rotation of major axis orientations for near-parabolic comets during the course of a single orbit, as discussed in Section 2.1.

3.3. Correlations between orbital elements

3.3.1. Correlations in energy and perihelion distance

We have seen that the tidal perturbation is weaker for increasing x, and this implies that any large-x comets that are made observable will preferentially have larger q. This correlation between large-x and large-q exists for the tide-alone perturbation, and it is extended to even larger values of x by a weak impulse. We show this correlation in Fig. 9 where contours of the comet flux are drawn for $\tau = 0$, before the shower commences, and $\tau = 1.25$ Myr, when the shower is near its peak. The correlation is observed throughout. Figure 10 shows the time evolution of the mean energy as a function of q, which further illustrates this effect.

3.3.2. Correlations in latitude and longitude

Figure 11 shows contours in the flux distribution, distributed in $\sin B$ and L, at $\tau = 0$ and 1.25 Myr. The arc of enhanced flux (the "track") corresponds to the stellar trajectory across the celestial sphere. We observe that the flux has minima at the poles and equator, where the galactic tidal torques are least - see Eq. (2). Note also the "well" in the shower flux at $B = 0$ and $L = 135°$ which is (counterintuitively) at closest approach to the Sun. The explanation is that in this aphelia direction velocity impulses to the Sun and comet are radial, and therefore the angular momentum impulse, Eq. (5), is zero. As the weak shower evolves, the distribution in aphelia directions maintains a near-constant full-width half-maximum of $\Delta L \approx 60°$ and a track length of $\approx 150°$.

We have seen in Sec. 3.3.1 that there is a correlation between energy and perihelion distance that exists for the tide-alone perturbation. During a weak stellar shower the correlation extends to higher values of x, for comets whose aphelia are localized on the celestial sphere along the stellar track, making it a three-fold correlation between energy, perihelion distance and aphelion direction. Thus, a defining characteristic of a weak stellar-induced comet shower is an overpopulated track of comet aphelia directions (with a gap in the

direction of closest approach) having preferentially larger values of x and q, which are correlated.

3.3.3. Another independent correlation

A fourth independent correlated variable can also be inferred and found in the analysis. In Fig. 1 we see that if the tidal perturbation is weak *but* non-negligible, (*i. e.*, for intermediate-A comets), and the stellar perturbation is weak *or* negligible, the comet can just barely enter the observable zone. Then $\mathbf{H^{obs}}$ will preferentially be opposed to $\mathbf{\Delta H^{tide}}$, *i.e.*, the variable

$$S \equiv \text{Sign}\left[\mathbf{H^{obs}} \cdot \mathbf{\Delta H^{tide}}\right] = -\text{Sign}\left[\cos\alpha^{obs}\ \dot{H}_{\phi}^{tide} + \sin\alpha^{obs}\ \dot{H}_{\theta}^{tide}\right] \tag{14}$$

will be equal to -1 more frequently than +1. Here α^{obs} is the observed orientation angle of $\mathbf{H^{obs}}$. This asymmetry occurs for the tide-alone perturbation and persists for weak stellar impulses in a distinctive way. The impulse *eliminates* the correlation in that part of phase space where the galactic tide alone partially refills the observable zone but the combined interaction completely refills it. The combined interaction *creates* the correlation in that part of observable phase space that is unfilled by the galactic tide alone, but is partially refilled by the combined tidal-impulse perturbation, *i. e.*, for intermediate-A. In Fig. 12 we show contour plots of $\left[\dot{N}(S<0) - \dot{N}(S>0)\right]$ distributed over x and q and with the same normalization as in Fig. 9. The latter shows the contours of $\left[\dot{N}(S<0) + \dot{N}(S>0)\right]$. The effect of the impulse on this correlation is found to be more clearly illustrated when $b_{\odot} > 50\ 000$ AU for weaker perturbations.

3.4. Further comparisons of weak showers with different parameters

Characteristics of showers of varying strengths and impact parameters have also been obtained. If only the time-dependent observable flux is desired, the number of cells can be reduced with little effect. Only cells with $0 \leq q < 5$ AU are needed and the number of cells in each angular variable can be reduced by a factor of 2 with a loss in accuracy of $< 3\%$. We present some of the details of the time-dependent observable

flux in Table 1. Included in the table are the stellar encounter parameters, the maximum flux, the flux at the last time step considered ($\tau = 5$ Myr), and the approximate times at maximum flux, half-maximum for the rise and for the decay of the shower. The final column lists a measure of the total shower flux, the flux-doubling time scale for observable comets

$$\delta\tau \equiv \int_0^{5\mathrm{Myr}} d\tau \left(\frac{\dot{N}(\tau) - \dot{N}_{tide}}{\dot{N}_{tide}} \right). \tag{15}$$

This is interpretable as the equivalent duration if the shower resulted in a constant observable flux twice as large as the tide-alone value.

The entries in Table 1 include a sampling of short range impulse cases with $b_\odot < 100\ 000$ AU and long range impulse cases with $b_\odot \geq 100\ 000$ AU. In the latter case the impulse strengths have been chosen to increase quadratically with $b_\odot$ to investigate the regime where a simple scaling law is possible for long range tidal impulses (see Eq. (6)).

Also included in Table 1 are the GL 710 baseline case details and the predictions for Algol ($M_\star/V_{rel} = 1.45$ $M_\odot$/km s^{-1} and $b_\odot = 490\ 000$ AU) which tidally impulsed the Solar System 6.9 Myr ago. Algol's relative velocity of 4 km s^{-1} makes it a borderline case for applicability of the impulse approximation, however.

The half-maximum duration of a weak stellar shower, $\approx 1.8 \pm 0.6$ Myr, is seen to be relatively insensitive to the stellar impulse parameters. The rise time of the shower is determined by the most tightly bound infalling comets brought into the observable zone by the impulse, while the decay time is determined by the least tightly bound impulsed outgoing comets for which the tide-alone perturbation is inefficient.

Along the celestial sphere the full-width half-maximum of the track narrows to $\approx 40°$ as $b_\odot \to 30\ 000$ AU. For long-range tidal impulses, no discernible track is found and the enhancement is widely distributed over the celestial sphere as is indicated by Eq. (6).

3.5. Comparisons with prior shower analyses

These results can be compared with the estimate of a 50% flux enhancement lasting for $\approx$ 2 Myr for *Earth-crossing* comets given in García Sánchez *et al.* (1999) for the best fit GL 710 parameters, $M_\star/V_{rel} = 0.043$ $M_\odot$/km s^{-1} and $b_\odot = 69\,000$ AU. Thus they estimate $\delta\tau_{\rm GS}(q < 1 \text{ AU}) \approx 1$ Myr while our analysis gives $\delta\tau(q < 5 \text{ AU}) \approx 0.2$ Myr. The different "observable" zone cannot explain the substantive difference in these results as our modeling indicates that flux enhancement is less at 1 AU than it is at 5 AU.

García Sánchez *et al.* (1999) also note that the tidal angular momentum impulse (see Eq. (6)) due to Algol was $\approx 2/3$ as strong as that due to the best fit GL 710 trajectory. Our analysis finds $\delta\tau(q < 5 \text{ AU}) \approx 0.05$ Myr which is $\approx 1/4$ that of our result for the best fit case of GL 710. Table 1 indicates that the tidal scaling law (Eq. (6)) is a reasonable approximation for impact parameters $b_\odot > 100\,000$ AU and that weak shower characteristics will be essentially constant for the same value of $M_\star/(V_{rel} {b_\odot}^2)$. However, it is found that $\delta\tau$ is not linearly proportional to this ratio in the tidal limit.

Biermann *et al.* (1983) inferred the existence of a weak stellar-induced comet shower in a study of 139 long-period comets. A clustering of aphelia had 27 comets (17 of 80 new and 10 of 59 intermediate energies) where only 6 would be expected if randomly distributed. Their analytic study concluded that $M_\star/V_{rel} = 0.025$ $M_\odot$/km s^{-1} and $b_\odot = 41\,500$ AU. The observed track size was $\approx 40° \times 70°$. From Fig. 2 we see that impulses that strong would give a peak flux of new comets $\approx 30\%$ over background as compared to the new flux observed at the present epoch which constitutes an enhancement over background of $\approx 20\%$. The mean encounter timescale for impulses of this strength or stronger is 29 Myr.

Heisler (1990) observed that 7 of 39 Class I and Class II new comets with $q < 2$ AU had $65 \leq x \leq 89$ and that essentially no comets should be found with $x > 60$ outside of showers. But she concludes that the large-x excess can be explained as due to (1) positive or negative error in the determination of x, (2) the failure to include nongravitational forces, and (3) contamination from comets that are not on their first

passage through the inner planetary region. All of these effects will tend to make comparisons of data and predictions more problematic. Problem (1) can be reduced by considering only Class I comets which have smaller errors in their energy determination than the lower quality orbit determinations of Class II comets. Problem (2) is associated mainly with small-q comets since outgassing increases with decreasing perihelion distance. A correlation between nominally hyperbolic original energies and small perihelion values has long been known (Marsden *et al.* 1978). Therefore this problem can be reduced by concentrating theoretical and observational comparisons to the range $q > 1$ AU. Problem (3) is not likely to be important since there are 9 Class I comets with $60 < x < 90$, no Class I comets with $90 < x < 135$, and 6 Class I comets with $135 < x < 180$. This is more readily understood as being due to effects (1) or (2), since they are associated with smaller energy dispersions than (3).

Heisler *et al.* (1987) (see also Heisler 1990) have performed the most notable simulations of the frequency and intensity of comet showers which included the galactic tidal interaction. They performed a long-time-scale Monte Carlo analysis in choosing the stellar type, impact parameter and velocity. Comet semimajor axes A = 10 000, 20 000 and 30 000 AU were considered. To get 100 comets to enter the loss cylinder ($\equiv$ 10 AU there), they had to follow $\approx 10^5$ individual comets employing a device of cloning token orbits. In particular, they concluded that stellar impulses were unable to increase the flux of comets with A = 30 000 AU. They found that for A = 10 000 and 20 000 AU the time averaged flux inside the loss cylinder was five times larger when an impulse-alone simulation was replaced by a tide+impulse simulation. The typical encounter interval for the strongest showers (defined there to be an increase in flux inside their 10 AU loss cylinder of a factor of 10 or more) was 100 - 150 Myr.

In a later work (Heisler *et al.* 1991) they described the sky distribution of a single strong shower with $M_\star/V_{rel}$ = 0.0375 $M_\odot$/km s^{-1} and $b_\odot$ = 20 000 AU. Only a single value of A = 20 000 AU was considered. They noted the gap in aphelia directions along the direction of closest approach. Although a larger value of galactic disk density was used there ($\langle\rho\rangle \approx$ 0.185 $M_\odot pc^{-3}$), the value of A considered was sufficiently small that the tide alone would be inefficient in refilling the loss cylinder. The width and length of the track was

comparable to that found here.

Weissman (1996) studied stellar-induced showers for $M_\star/V_{rel} = 0.020$ and 0.033 $M_\odot$/km s^{-1} over a range $b_\odot$ = 2 000 - 100 000 AU using a loss cylinder radius of 50 AU, substantially larger than in Heisler *et al.* or in this work. He was most interested in the fraction of the Oort cloud lost to various end states; direct ejection, loss cylinder filling, and aphelia pumping to > 200 000 AU where galactic tides could strip the comet from the cloud. In a detailed illustration with $b_\odot$ = 10 000 AU, he obtained the sky distribution of comets perturbed to $q < 10$ AU and concluded that it would be near-isotropic. The expected gaps in the directions $\pm\mathbf{b}_\odot$ were not noted. He concludes that we are not now in a (strong) shower.

4. SUMMARY AND CONCLUSIONS

We have developed an efficient semi-analytic mapping procedure to determine the response of outer Oort cloud comets to the tidal perturbation of the galactic force and weak impulsive perturbations of passing stars. It is demonstrated that significant errors are made when one separately analyzes the response of the comet cloud to the galactic tide and to the stellar impulse, and then superposes the flux from the two analyses. The galactic and stellar perturbations must be properly superposed into a single analysis to obtain correct predictions.

The frequency and flux characteristics of a weak stellar-induced comet shower has been obtained over a wide range of impact parameters and impulse strengths. A weak shower fingerprint includes an enhanced comet flux along a broad ($\approx 40° - 60°$) track of aphelia directions extending $\approx 150°$ along the celestial sphere. Comets along this track will preferentially show a four-fold correlation of orbital elements.

Oort cloud comet showers with flux < 1.2× background will be difficult to discern from the observations presently available if only the energy range $x < 70$ is significantly affected by the impulse. We estimate that the mean encounter timescale of impulses having $b_\odot \geq$ 30 000 AU and producing a flux at least 20% above background is $\geq$ 15 Myr. Since a weak stellar-induced comet shower will be manifest in the observable Oort

cloud comet flux distributions $\approx 0.8 \pm 0.4$ Myr after the impulse, and will be significantly reduced $\approx 2.6 \pm 1$ Myr after the impulse, it is somewhat unlikely that we should presently be in a detectable weak stellar shower.

The 1σ lower limit of the closest approach for the upcoming Gliese 710 impulse would yield a peak observable flux $\approx 1.4\times$ the present background flux. The Solar System typically encounters a star with $M_\star/V_{rel} \geq 0.043$ $M_\odot$/km s^{-1} and a closest approach $b_\odot \leq 45\ 000$ AU with a mean encounter timescale of 67 Myr. But the path has a sufficiently large uncertainty that a wide range of shower intensities is possible.

Is there evidence for a weak shower other than the Biermann shower? Matese *et al.* (1999) concluded that there was statistically significant evidence for a four-fold correlated signal in the observed new Class I comet data base (Marsden and Williams 2000), amounting to a flux enhancement of $\approx 25\%$. Claims that such a signal might be the result of small sampling, bad data or observational selection effects remain unsupported by analysis and have been argued against (Matese *et al.* 1998). But their observed overpopulated track differs in one significant characteristic from those modeled here. Its length ($\approx 270°$) and width ($\approx 25°$) are not consistent with those found for comparable showers due to stellar impulses of short range or long range. Matese *et al.* (1999) suggested that the longer, narrower track could be created by a bound Jovian mass perturber in the Oort cloud, and a corresponding study of that conjecture is underway.

ACKNOWLEDGMENTS

Useful discussions with Daniel Whitmire, Ray Reynolds and Morris Podolak are appreciated. Constructive reviews by Luke Dones and Paul Wiegert helped to improve the manuscript. JJM acknowledges a NASA-AAS Small Research Grant and a NASA-ASEE Summer Faculty Fellowship at Ames Research Center. JJL received support from Planetary Geology and Geophysics Grant #344-30-50-01.

Figure Captions

Figure 1. The mapping model showing angular momentum phase space after displacement by the perturbations. Filled phase space is the light gray region. The prior distribution is filled outside the loss cylinder boundary and empty inside. All prior phase space points, filled and empty, are uniformly displaced by the stellar impulse and by the tidal torque ($\mathbf{\Delta H} = \mathbf{\Delta H^{impulse}} + \mathbf{\Delta H^{tide}}$). If the total displacement moves the prior loss cylinder boundary inside or beyond the observable zone (small circle), the combined interaction can make comets observable (dark gray region) for this set of orbital elements B, L, x, τ. The orientation angle of $\mathbf{H^{obs}}$ defines α^{obs}.

Figure 2. The peak flux, normalized to the tide-alone flux, as a function of closest approach distance and stellar impulse strength.

Figure 3. Cumulative mean encounter frequency, ξ defined in Eq. (12), as a function of closest approach distance and stellar impulse strength. The results are for all impulses strengths $> M_\star/V_{rel}$ and closest approach $< b_\odot$. Decreasing dash length correspond to loci for mean encounter timescales ξ^{-1} = 1, 2, 5, 10, 20, 50, 100 and 200 Myr. The median time to the next encounter is 0.693 ξ^{-1}.

Figure 4. Instantaneous flux of observable comets ($q < 5$ AU), integrated over all other orbital elements and normalized to the tide-alone rate for our standard test case ($M_\star/V_{rel} = 0.043$ $M_\odot$/km s^{-1}, closest approach $\mathbf{b}_\odot$= 45 000 AU at galactic longitude $L = 135°$, with V_{rel} along the galactic z axis). Solid curve → flux from superposed perturbations of the star and galaxy (realistic simulation). Dotted curve → superposed flux from separate analyses (artificial analysis, for comparison purposes).

Figure 5. The fractional efficiency, f, for refilling the observable part of the loss cylinder phase space for the shower whose flux is shown in Fig. 4). Top panel, superposed flux from separate analyses; bottom panel, flux from superposed perturbations. Both are plotted as a function of the original orbital energy parameter, x. Increasing dash length indicates the arrival times τ = 0, 0.6, 1.25, 2.0, 3.5 and 5 Myr. Not all times are distinguishable in the lower panel. Note that values of f greater than unity are unphysical artifacts of the superposed-flux model.

Figure 6. Time-dependent flux of observable comets, distributed in energy and normalized to the peak for the $\tau = 0$ curve. Results are for the baseline shower shown in Fig. 4 (solid curve) and Fig. 5 (bottom panel). Dash length as in Fig. 5.

Figure 7. Time-dependent flux of observable comets for the baseline shower, distributed in perihelion distance and normalized to the Earth-crossing flux at $\tau = 0$. Dash length as in Fig. 5.

Figure 8. Time-dependent flux of observable comets for the baseline shower, distributed in (a) galactic latitude, and (b) galactic longitude, normalized to the peaks for the $\tau = 0$ curves. Dash length as in Fig. 5.

Figure 9. Flux distribution in energy and perihelion distance for the baseline shower, normalized to the peak flux during the shower. (a) Galactic tide alone, $\tau = 0$. (b) Near shower maximum, $\tau = 1.25$ Myr.

Figure 10. Time-dependent mean energy (sliding average over 1 AU intervals in q) as a function of perihelion distance for the baseline shower. Dash length as in Fig. 5.

Figure 11. Flux distribution in solid angle, $d\Omega \equiv d \sin B \; dL$, for the baseline shower, normalized to the peak flux during the shower. (a) Galactic tide alone, $\tau = 0$. (b) Near shower maximum, $\tau = 1.25$ Myr.

Figure 12. Distribution in the dynamical signature S, defined in Eq. (14) and normalized as in Fig. 9, for the baseline shower. (a) Galactic tide alone, $\tau = 0$. (b) Near shower maximum, $\tau = 1.25$ Myr.

REFERENCES

Biermann, L., W.F. Huebner, and R. Lüst 1983. Aphelion clustering of "new" comets: Star tracks through Oort's cloud. *Proc. Natl. Acad. Sci. USA* **80**, 5151-5155.

Byl, J. 1983. Galactic perturbations on nearly parabolic comet orbits. *Moon Planets* **29**, 121-137.

Duncan, M., T. Quinn, and S. Tremaine 1987. The formation and extent of the Solar System comet cloud. *Astron. J.* **94**, 1330-1338.

Fernandez, J. 1981. New and evolved comets in the Solar System. *Astron. Astrophys.* **96**, 26-35.

García Sánchez, J., R. A. Preston, D. L. Jones, P. R. Weissman, J. F. Lestrade, D. W. Latham, and R.P. Stefanik 1999. Stellar encounters with the Oort cloud based on *HIPPARCOS* data. *Astron. J.* **117**, 1042-1055.

Heisler, J. 1990. Monte Carlo simulations of the Oort comet cloud. *Icarus* **88**, 104-121.

Heisler, J., and S. Tremaine 1986. Influence of the galactic tidal field on the Oort cloud. *Icarus* **65**, 13-26.

Heisler, J., S. Tremaine, and C. Alcock 1987. The frequency and intensity of comet showers from the Oort cloud. *Icarus* **70**, 269-288.

Heisler, J., S. Tremaine, P. Weissman, and R. Greenberg 1991. Sky distribution of Oort cloud comets during and outside of showers. *Lunar and Planetary Science Conference* **XXII**, 553-554.

Holmberg, J., and C. Flynn 2000. The local density of matter mapped by *HIPPARCOS. MNRAS* **313**, 209-216.

Levison, H. F., L. Dones, and M. J. Duncan 2001. The origin of Halley-type comets: Probing the inner Oort cloud. Astron. J. **121**, 2253-2267.

Marsden, B. G., Z. Sekanina, and E. Everhart 1978. New Osculating orbits for 110 comets and analysis of original orbits for 200 comets. *Astron. J.* **83**, 64-71.

Marsden, B. G., and G. V. Williams 2000. *Catalogue of Cometary Orbits, 13th Ed.* Smithsonian Astrophysical Observatory, Cambridge, MA.

Matese, J. J., and P. G. Whitman 1992. A model of the galactic tidal interaction with the Oort comet cloud. *Cel. Mech. Dyn. Astron.* **54**, 13-36.

Matese, J. J., and D. P. Whitmire 1996. Tidal imprint of distant galactic matter on the Oort comet cloud. *Ap. J.* **472**, L41-L43.

Matese, J. J., P. G. Whitman and D. P. Whitmire 1998. Oort cloud comet perihelion asymmetries: galactic tide, shower or observational bias? *Cel. Mech. Dyn. Astron.* **69**, 77-88.

Matese, J. J., P. G. Whitman and D. P. Whitmire 1999. Cometary evidence of a massive body in the outer Oort cloud. *Icarus* **141**, 354-366.

Merrifield, M. R. 1992. The rotation curve of the Milky Way to 2.5 R_o from the thickness of the HI layer. *Astron J.* **103**, 1552-1563.

Oort, J. H. 1950. The structure of the cloud of comets surrounding the Solar System, and a hypothesis concerning its structure. *Bull. Astron. Inst. Neth.* **11**, 91-110.

Stern, S. A., and P. R. Weissman 2001. Rapid collisional evolution of comets during the formation of the Oort cloud. *Nature* **409**, 589-590.

Weissman, P. R. 1996. Star passages through the Oort cloud. *Earth Moon Planets* **72**, 25-30.

Wiegert, P., and S. Tremaine 1999. The evolution of long-period comets. *Icarus* **137**, 84-122.

Wolfram Research 1999. *Mathematica*, 4th Ed. Cambridge University Press.

Table 1: **Observable flux time dependence for weak comet showers.**
The impact parameter scale is 10^3 AU, the impulse strength scale is $M_\odot$/km s^{-1}, and all time scales are Myr. The bold face entry at $b_\odot$ = 45 000 AU is for the baseline case of GL 710, the italicized entry at $b_\odot$ = 69 000 AU is for the best fit trajectory of GL 710, and the italicized entry at $b_\odot$ = 490 000 AU is for the best fit trajectory of Algol.

Encounter	parameters	Observable	flux	Timing	of	shower	Flux-doubling time
$b_\odot$	$M_\star/V_{rel}$	$\frac{\dot{N}(max)}{\dot{N}_{tide}}$	$\frac{\dot{N}(5\mathrm{Myr})}{\dot{N}_{tide}}$	$\tau(rise)$	$\tau(max)$	$\tau(decay)$	$\delta\tau$
30	0.01	1.11	0.99	0.50	0.80	1.20	0.03
30	0.02	1.39	0.98	0.45	0.80	1.45	0.40
30	0.03	1.72	0.98	0.40	0.80	1.70	0.96
40	0.01	1.05	1.00	0.80	1.25	1.70	0.03
40	0.02	1.19	1.00	0.75	1.20	1.90	0.23
40	0.03	1.37	1.00	0.70	1.10	1.95	0.52
40	0.05	1.83	1.00	0.65	1.05	2.10	1.29
40	0.07	2.26	1.00	0.60	1.05	2.25	2.24
45	**0.043**	**1.41**	**1.00**	**0.78**	**1.33**	**2.39**	**0.72**
50	0.03	1.18	1.01	0.95	1.60	2.65	0.31
50	0.05	1.38	1.01	0.80	1.50	2.70	0.73
50	0.07	1.62	1.02	0.80	1.40	2.70	1.24
50	0.09	1.89	1.02	0.70	1.30	2.70	1.84
60	0.03	1.08	1.01	1.25	1.85	3.05	0.18
60	0.05	1.20	1.02	1.10	1.80	3.00	0.44
60	0.07	1.33	1.02	0.95	1.65	3.00	0.73
60	0.09	1.48	1.03	0.85	1.55	3.00	1.07
69	*0.043*	*1.08*	*1.01*	*1.25*	*2.45*	*3.50*	*0.19*
70	0.05	1.11	1.02	1.30	2.50	3.40	0.24
70	0.07	1.18	1.02	1.15	1.80	3.35	0.42
70	0.09	1.27	1.03	1.00	1.75	3.25	0.64
80	0.07	1.11	1.02	1.35	2.50	3.50	0.25
80	0.09	1.16	1.02	1.10	2.40	3.50	0.39
50	0.05	1.38	1.01	0.80	1.50	2.70	0.73
100	0.20	1.26	1.04	1.15	2.20	3.50	0.66
200	0.80	1.23	1.04	1.20	2.40	3.60	0.60
300	1.80	1.23	1.04	1.20	2.40	3.60	0.59
490	*1.45*	*1.03*	*1.01*	*1.45*	*2.50*	*3.15*	*0.05*

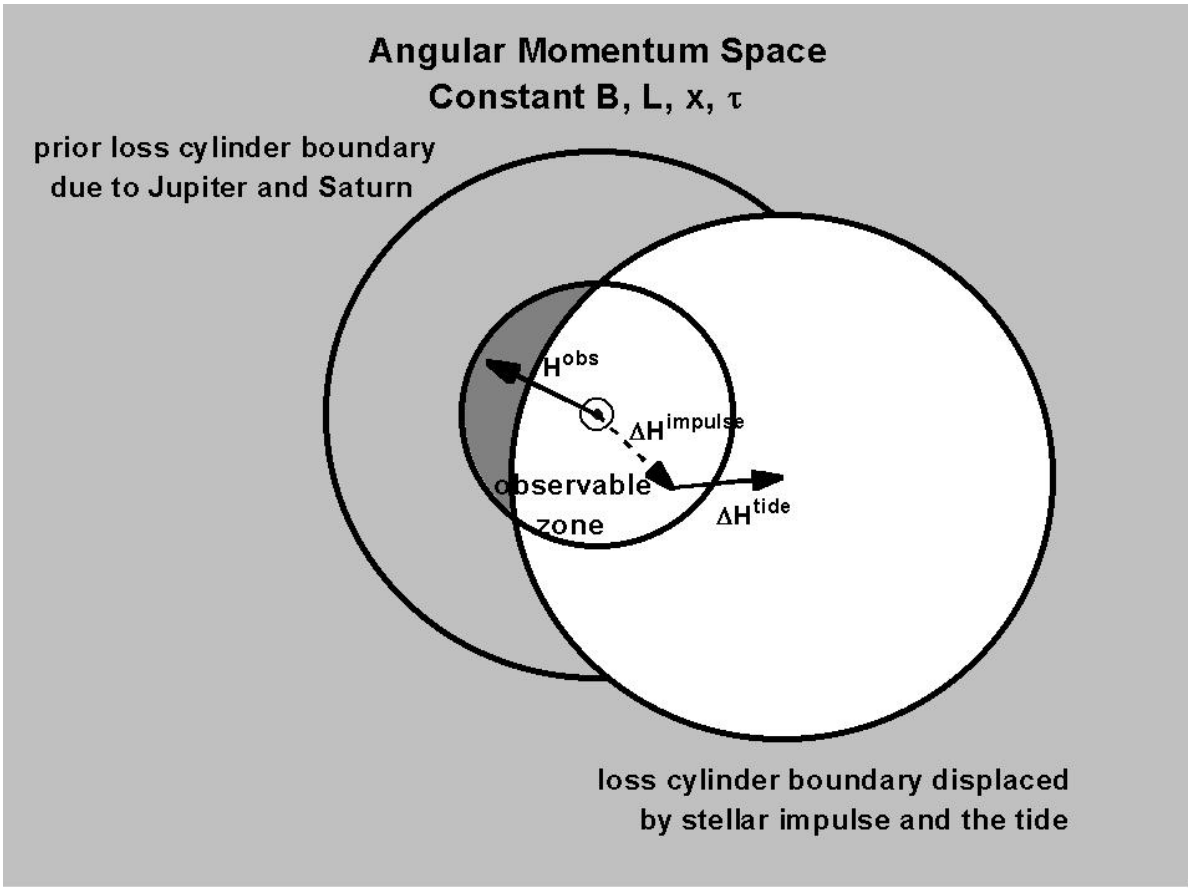
Angular Momentum Space
Constant B, L, x, τ
prior loss cylinder boundary
due to Jupiter and Saturn
H^obs
ΔH^impulse
observable
zone
ΔH^tide
loss cylinder boundary displaced
by stellar impulse and the tide

Fig. 1.—

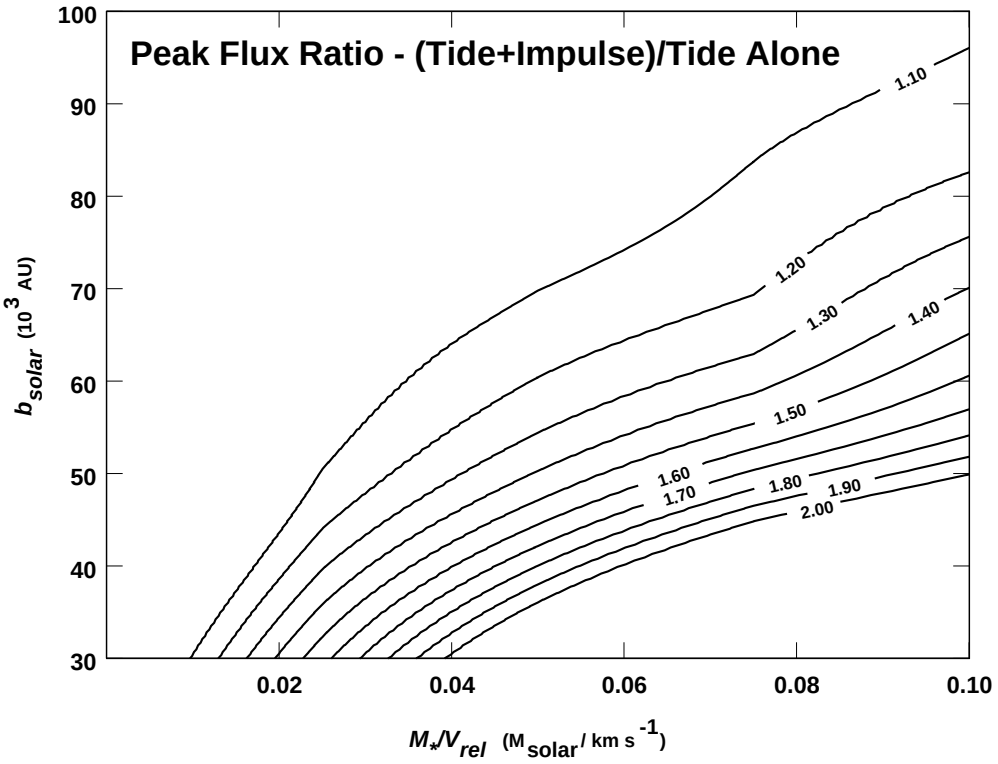
Peak Flux Ratio - (Tide+Impulse)/Tide Alone
1.10
1.20
1.30
1.40
1.50
1.60
1.70
1.80
1.90
2.00
100
90
80
70
60
50
40
30
0.02
0.04
0.06
0.08
0.10
b_solar (10^3 AU)
M*/V_rel (M_solar / km s^-1)

Fig. 2.—

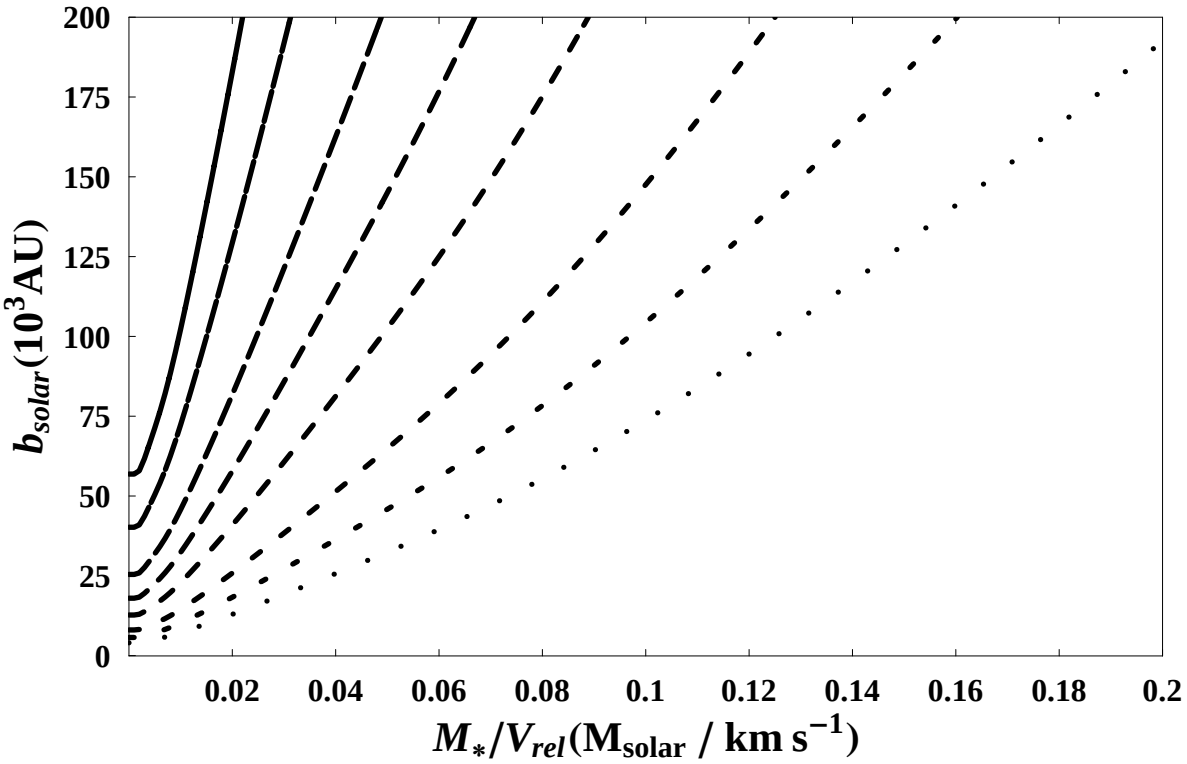
200
175
150
125
100
75
50
25
0
$b_{solar}(10^3 \mathrm{AU})$
0.02
0.04
0.06
0.08
0.1
0.12
0.14
0.16
0.18
0.2
$M_*/V_{rel}(\mathrm{M_{solar}}$ / km $\mathrm{s^{-1}})$

Fig. 3.—

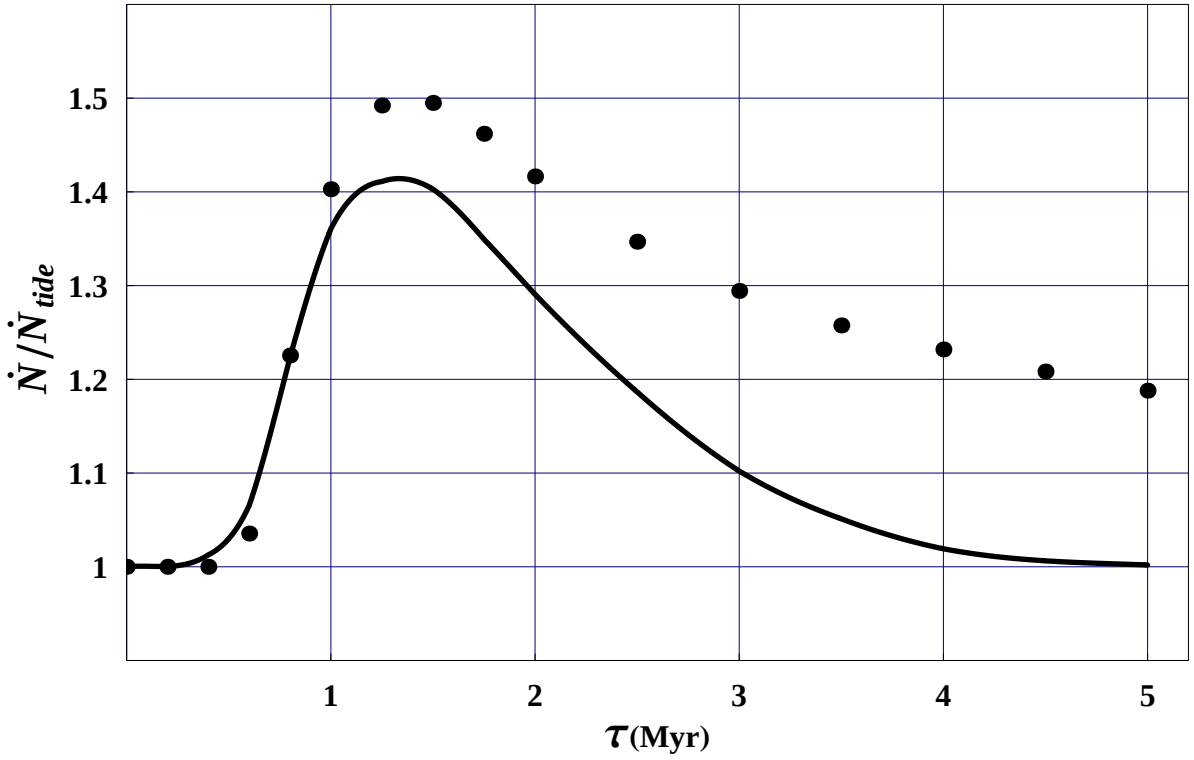

Fig. 4.—

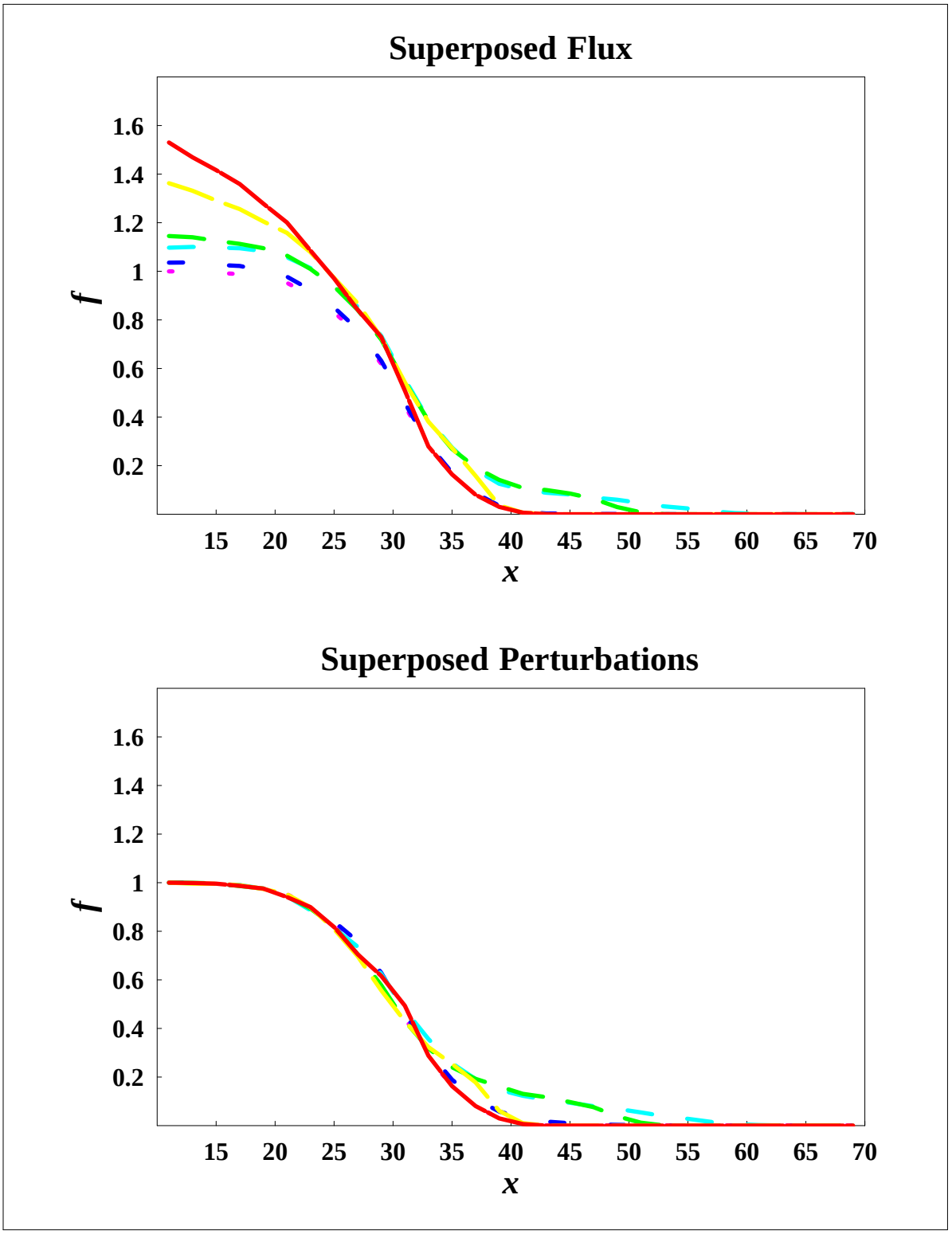
Superposed Flux
f
x
1.6
1.4
1.2
1
0.8
0.6
0.4
0.2
15
20
25
30
35
40
45
50
55
60
65
70
Superposed Perturbations
f
x
1.6
1.4
1.2
1
0.8
0.6
0.4
0.2
15
20
25
30
35
40
45
50
55
60
65
70

Fig. 5.—

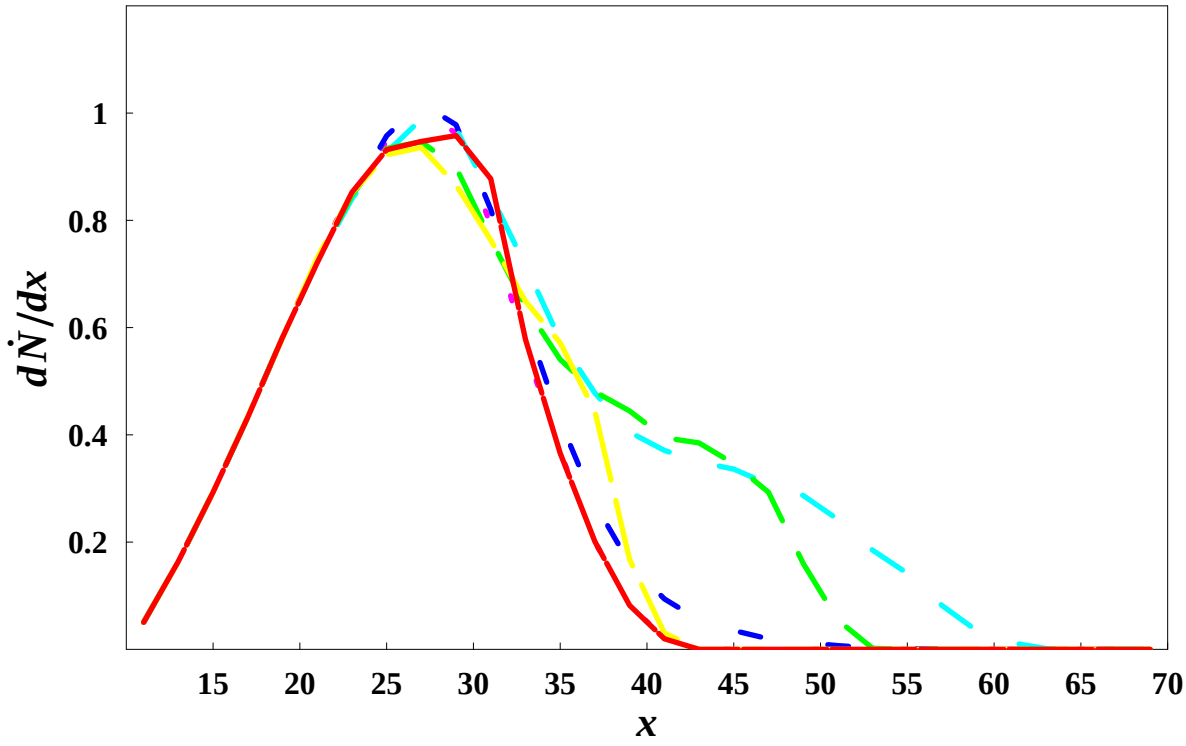

Fig. 6.—

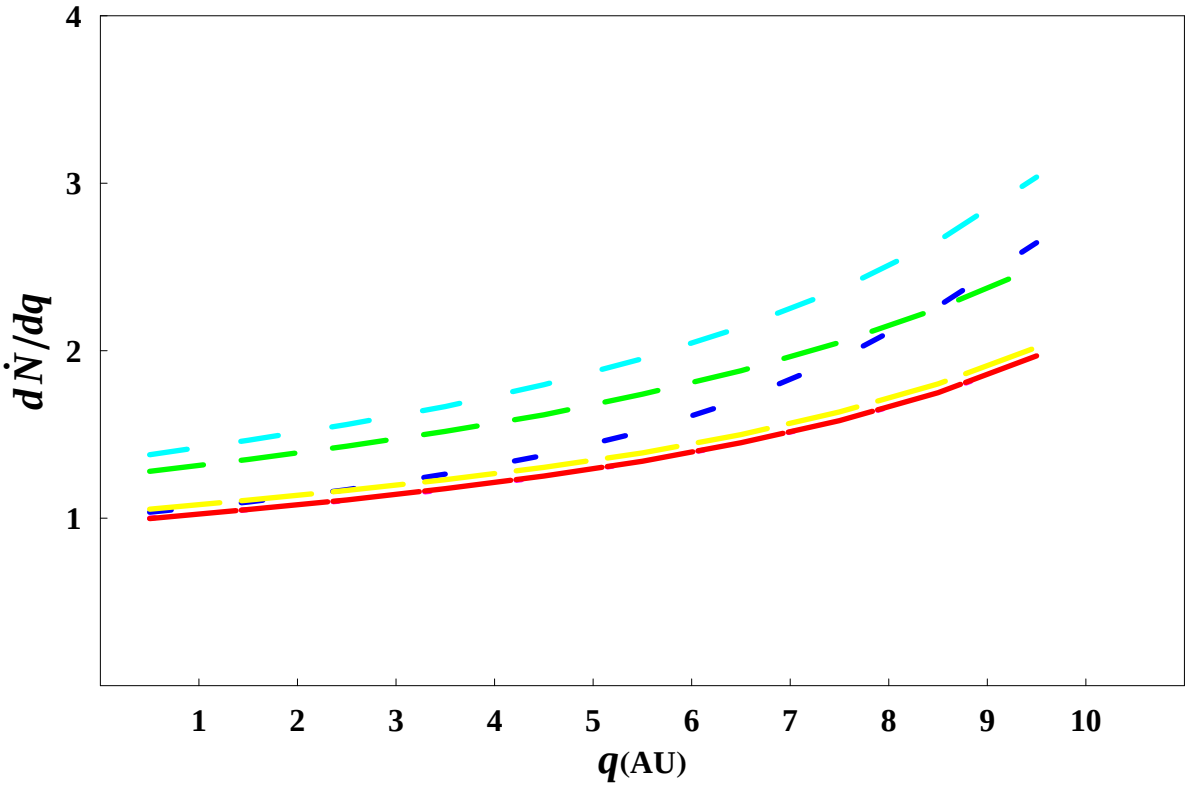

Fig. 7.—

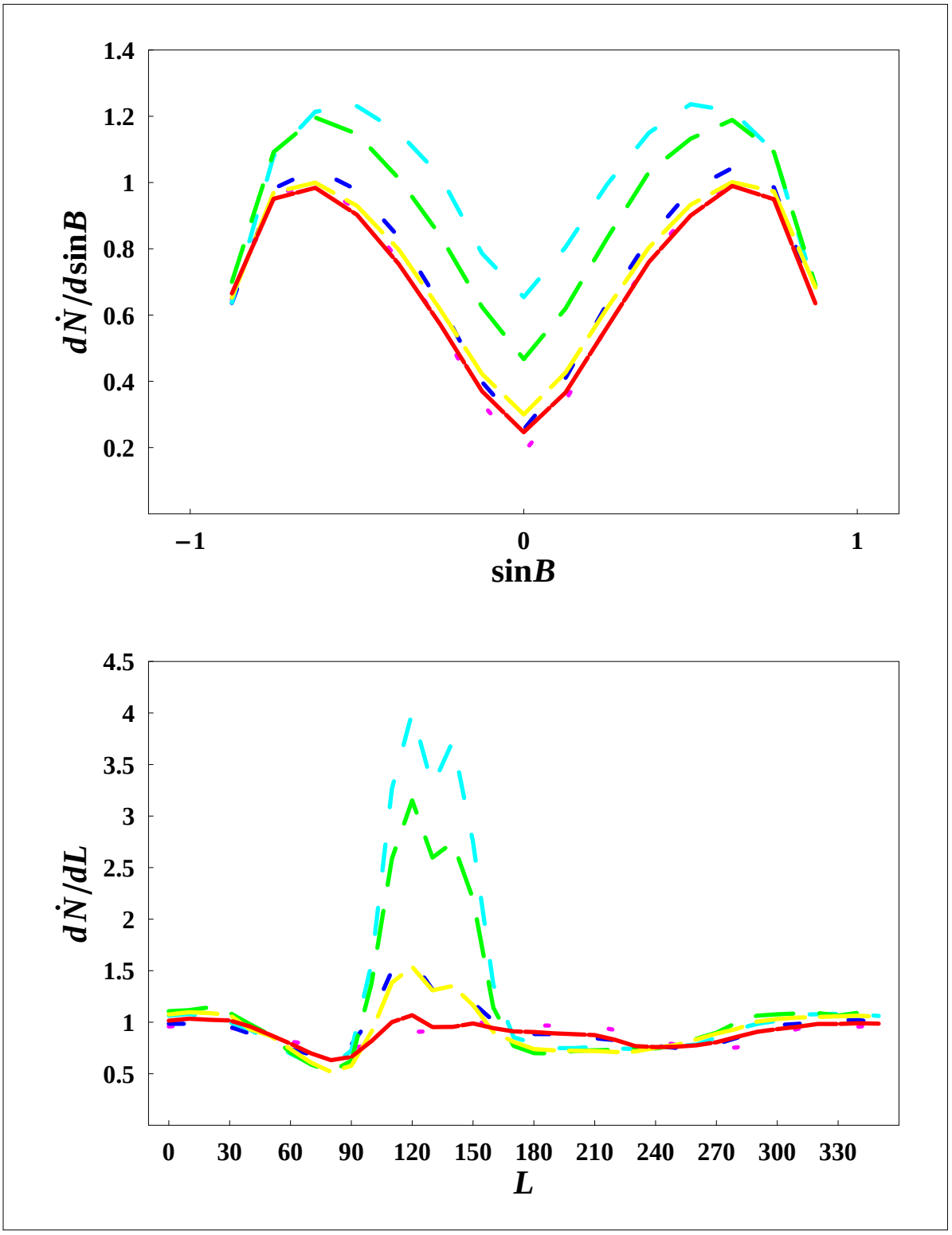
1.4
1.2
1
0.8
0.6
0.4
0.2
$d\dot{N}/d\sin B$
−1
0
1
$\sin B$
4.5
4
3.5
3
2.5
2
1.5
1
0.5
$d\dot{N}/dL$
0
30
60
90
120
150
180
210
240
270
300
330
L

Fig. 8.—

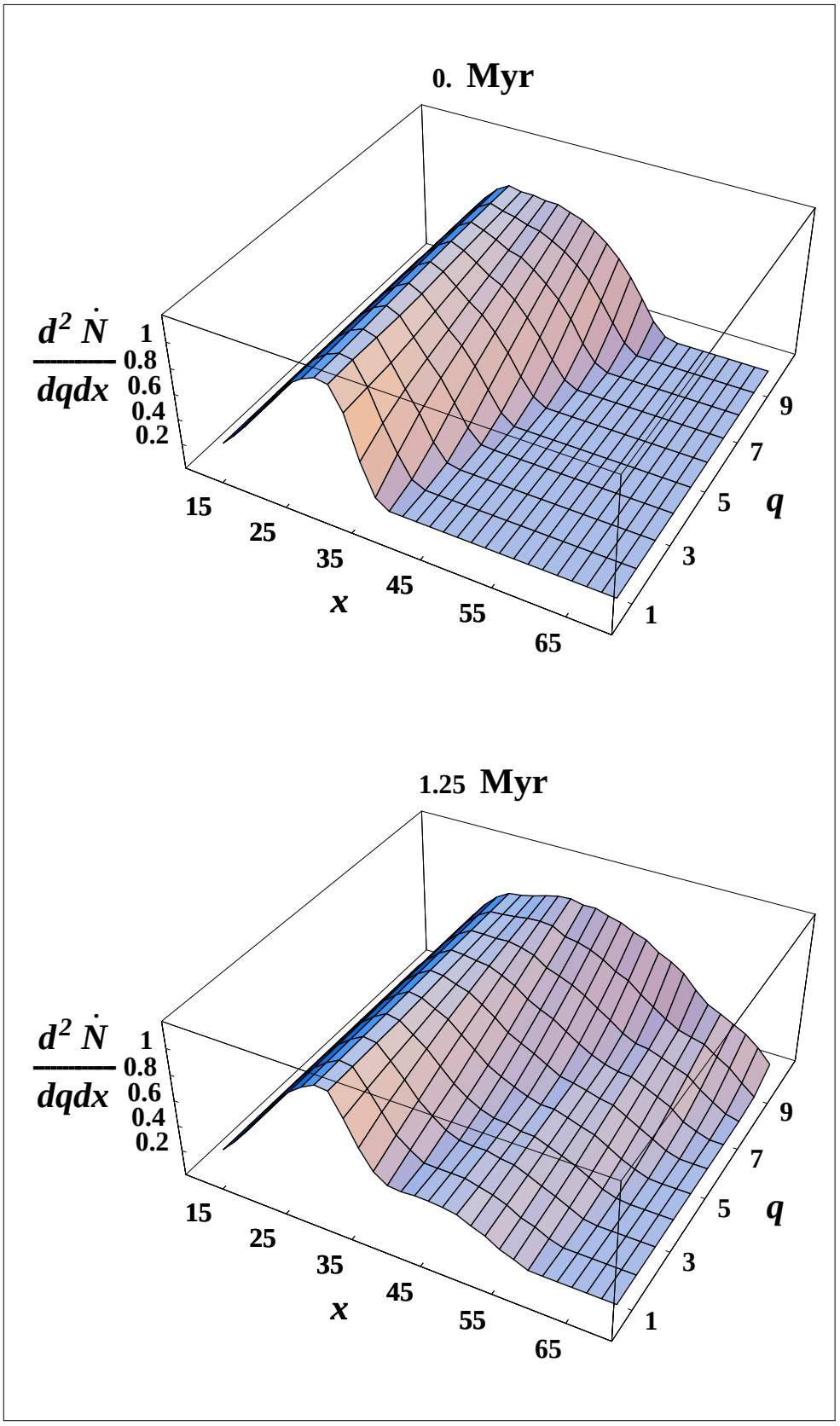
0. Myr
$\frac{d^2 \dot{N}}{dqdx}$
1
0.8
0.6
0.4
0.2
15
25
35
45
55
65
x
1
3
5
7
9
q
1.25 Myr
$\frac{d^2 \dot{N}}{dqdx}$
1
0.8
0.6
0.4
0.2
15
25
35
45
55
65
x
1
3
5
7
9
q

Fig. 9.—

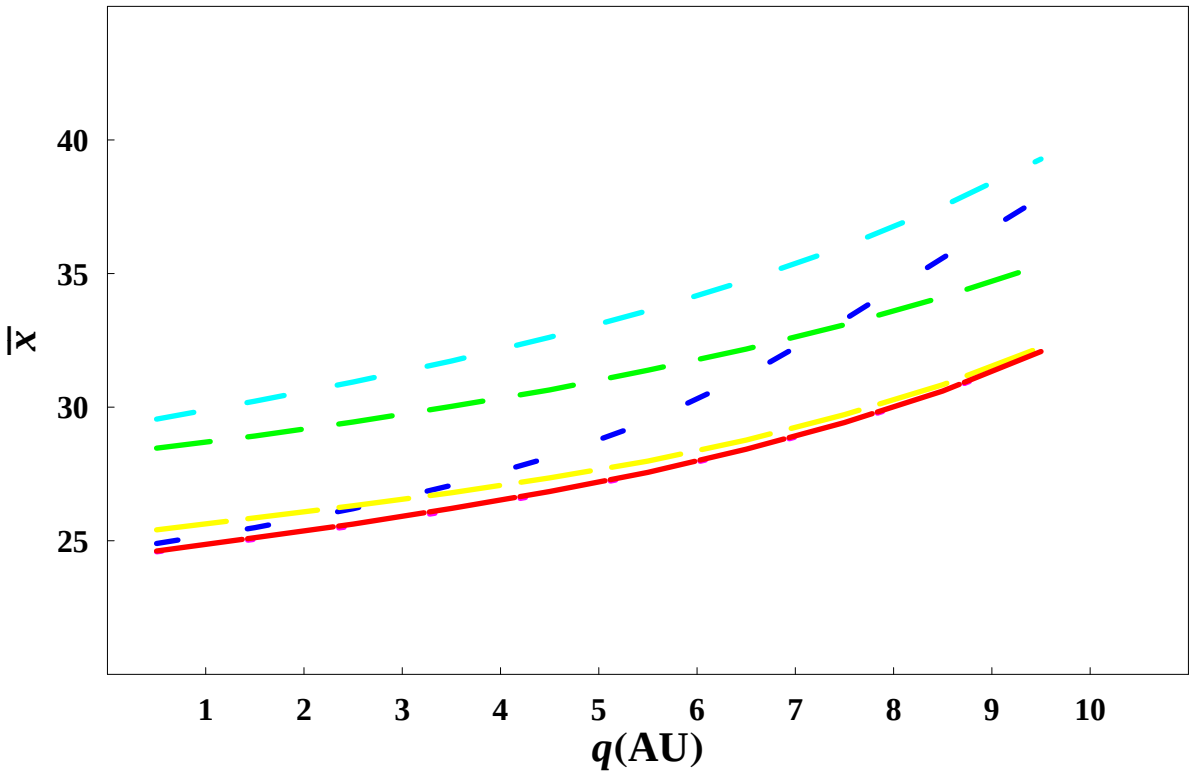

Fig. 10.—

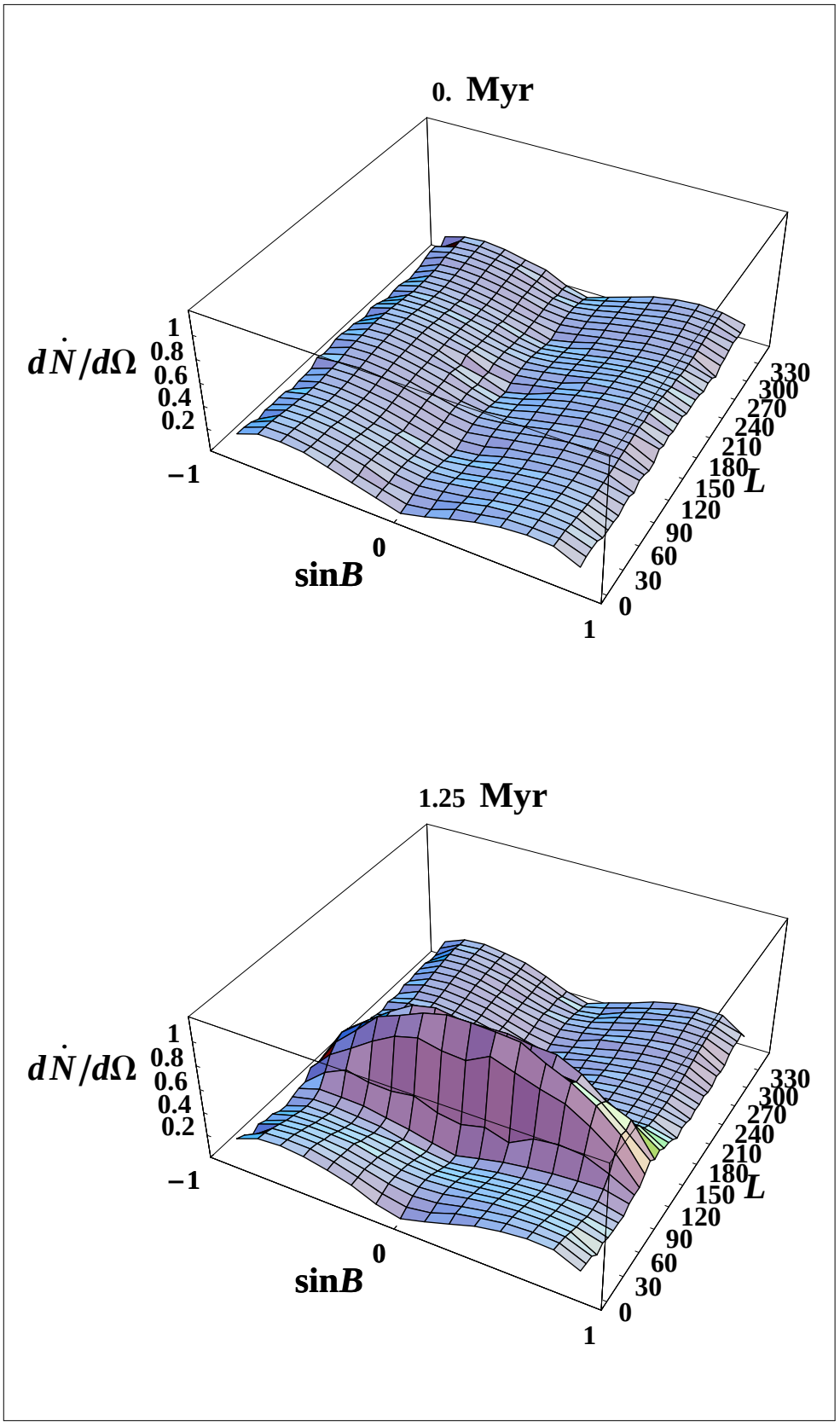
0. Myr
dṄ/dΩ
1
0.8
0.6
0.4
0.2
−1
sinB
0
1
L
0
30
60
90
120
150
180
210
240
270
300
330
1.25 Myr
dṄ/dΩ
1
0.8
0.6
0.4
0.2
−1
sinB
0
1
L
0
30
60
90
120
150
180
210
240
270
300
330

Fig. 11.—

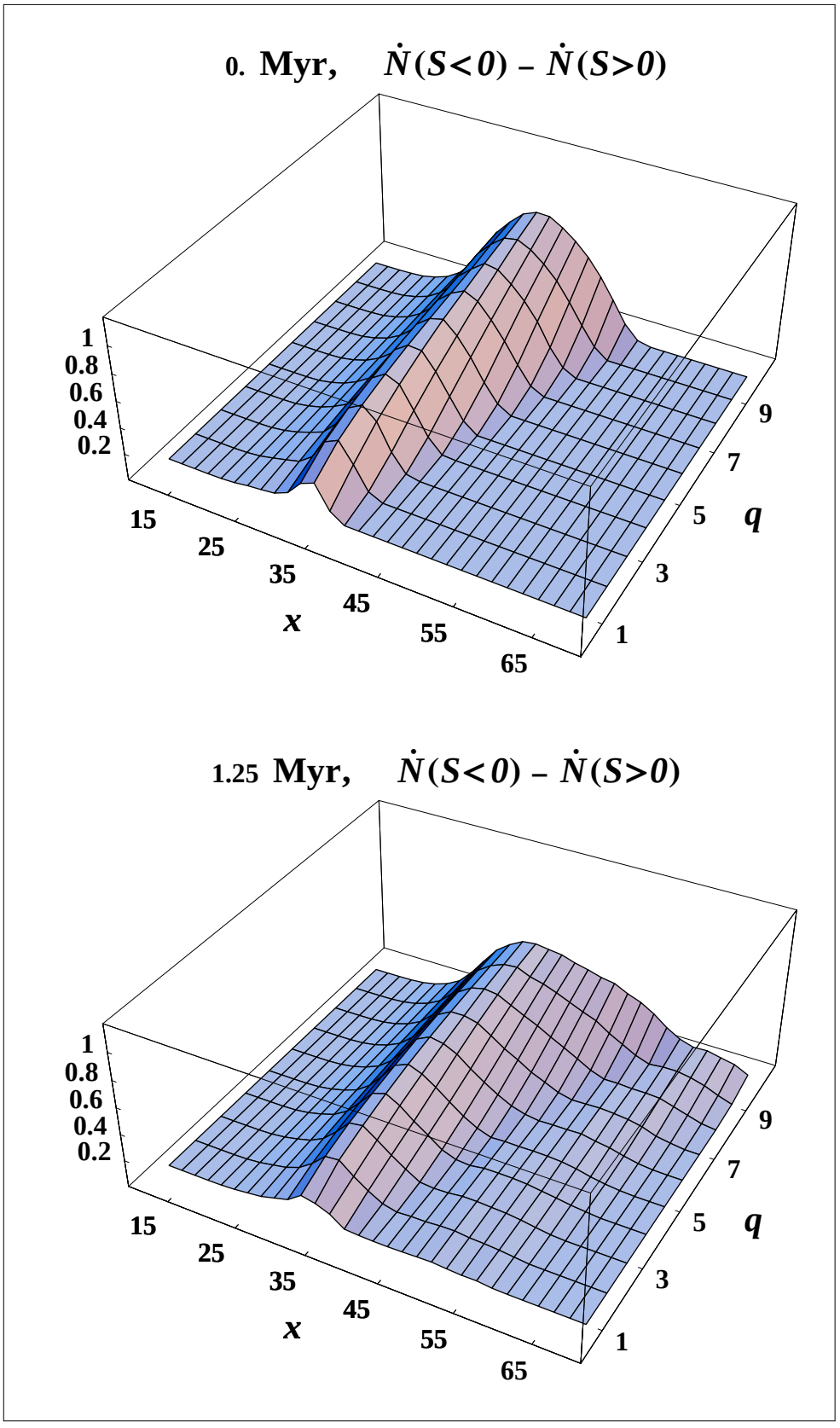
0. Myr, $\dot{N}(S<0) - \dot{N}(S>0)$
1
0.8
0.6
0.4
0.2
15
25
35
45
55
65
x
1
3
5
7
9
q
1.25 Myr, $\dot{N}(S<0) - \dot{N}(S>0)$
1
0.8
0.6
0.4
0.2
15
25
35
45
55
65
x
1
3
5
7
9
q

Fig. 12.—